Magnitude and phase activation detection in functional MRI time series

Daniel W. Adrian* Ranjan Maitra† Daniel B. Rowe‡

Abstract

Functional MRI is a popular noninvasive technique for mapping brain regions activated by specific brain functions. However, as fMRI measures brain activity indirectly through blood flow, the so-called "brain or vein" problem refers to the difficulty in determining whether measured activation corresponds to (desired) brain tissue or (undesired) large veins, which may be draining blood from regions with activated neurons. Now, fMRI data consist of both magnitude and phase components (*i.e.*, it is complex-valued), but in the vast majority of statistical analyses, only the magnitude data is utilized. However, while activation in the magnitude component can come from both "brain or vein", previous work has demonstrated that activation in the phase component "discriminates" between the two: phase activation occurs in voxels with large, oriented vessels but not in voxels with small, randomly oriented vessels immediately adjacent to brain tissue. Following this motivation, we have developed a model that allows for activation in magnitude and phase, one more general than those previously proposed.

Key Words: complex-valued data, maximum likelihood, neurosurgical planning, signal-to-noise ratio, von-Mises distribution

1. Introduction

Functional magnetic resonance imaging (fMRI) is a prominent non-invasive modality for studying human brain function. It is built upon the Blood Oxygen Level Dependent (BOLD) contrast (Bandettini et al., 1993; Belliveau et al., 1991; Kwong et al., 1992; Ogawa et al., 1990), where firing neurons lead to changes in the blood oxygen levels of neighboring vessels, and the magnetic resonance (MR) signal fluctuates due to the differing magnetic susceptibilities of oxygenated and deoxygenated hemoglobin (Lazar, 2008). Scientists can gain insight on the functional structures of the brain by analyzing time courses of MR images acquired while a subject performs a designed series of tasks.

The acquired fMRI data at each voxel and time-point is complex-valued, containing real and imaginary (or equivalently, magnitude and phase) components. This is a result of how the data is collected: the originally measured, complex-valued k-space data (Brown et al., 1982; Ljunggren, 1983; Tweig, 1983) consists of the different frequency contributions to the signal from each voxel resulting from magnetic field gradients (Jezzard and Clare, 2001). Then, the application of the inverse Fourier transform (Jain, 1989), a complex-valued operation, on the k-space data separates these frequencies and thus localizes each voxel's measurements.

However, statistical analysis of fMRI data is almost always on the magnitude data alone, in which case the acquired phase data is discarded (Lee et al., 2007; Rowe and Logan, 2004) and the focus is on task-related magnitude changes (Rowe and Logan, 2005). This practice has carried over from structural MRI – which focuses on determining brain anatomy, not function. But the including the phase information has proved useful in several ways.

*Department of Statistics, Grand Valley State University, Allendale, MI 49401-9403
†Department of Statistics, Iowa State University, Ames, IA 50011-1090
‡Department of Mathematical and Statistical Sciences, Marquette University, Milwaukee, WI 53233

First, the phase information is useful in visualizing anatomical brain structures, in vivo, at a level previously only available from cadavers (Reichenbach, 2012). This imaging first focused on cerebral venous vessels — *i.e.*, MR venography (Reichenbach et al., 1997) – and was extended to brain structures such as deep brain nuclei, white matter fiber bundles, and tissue iron deposits, in what came to be known as susceptibility weighted imaging (Haacke et al., 2004; Rowe and Haacke, 2009).

Second, including the phase has been shown to improve activation detection in fMRI, even for magnitude-only task-related activation. That is, models for complex-valued time series with task-related changes in the mean magnitude but assuming constant phase have shown improved activation detection over models that utilize the magnitude-only data (Adrian et al., 2018; Nan and Nowak, 1999; Rowe, 2005b; Rowe and Logan, 2004). The largest differences between complex-valued and magnitude-only data-based activation occur at low signal-to-noise ratios (Rowe and Logan, 2004) and when there is a correlation between the real and imaginary error time series (Adrian et al., 2018), the latter which is induced by spatial smoothing (Karaman et al., 2014; Nencka et al., 2009).

Most compelling, phase task-related activation is useful in the so-called "brain or vein" problem (Frahm et al., 1994). This problem seeks to determine whether BOLD signal changes are dominated by (desired) grey matter or (undesired) macrovasculature, such as the cortical cerebral veins and larger pial veins. In this context, Menon (2002) distinguishes between voxels containing macrovascular veins and those with only microvascular veins; the former have vessels that can be considered essentially linear and oriented while the venuoles in the latter are more or less randomly oriented. While magnitude task-related changes occur in both types of voxels, Hoogenrad et al. (1998) presents theory and data supporting that a task-related phase change is expected for in macrovascular voxels but not in microvascular ones.[1]

Menon (2002) proposes a method for suppressing macrovascular BOLD signals via the linear relationship between magnitude and phase changes. Nencka and Rowe (2007) show that this method can at times overcorrect and induce negative activation and also illustrate how the Rowe and Logan (2004) constant-phase model can be used to bias against voxels with task-related phase changes, which is demonstrated in experimental data in Nencka et al. (2008).

An important application of fMRI is presurgical planning of invasive neurosurgical procedures (Pillai, 2010). For example, experimental paradigms incorporating fingertapping, hand brushing, or sponge squeezing are used to locate the functional central sulcus, the region responsible for hand function in healthy adults, prior to neurosurgery (Lee et al., 1998, 1999). However, the presence of a draining vein in the central sulcus (Duvernoy, 1999) makes distinguishing pre- from postcentral gyrus activity extremely difficult (Menon, 2002), complicating neurosurgical planning. This context provides our motivation for developing statistical models for detecting magnitude and phase activation from complex-valued fMRI time series.

1.1 Statistical models for detecting magnitude and phase activation

Statistical models for detecting magnitude and phase activation have two major groups, depending on whether the real and imaginary means are phase coupled. To illustrate, we introduce notation, focusing on a single voxel time series (and thus suppressing voxel-related subscripts). We denote the real and imaginary measurements at time t by y_{Rt} and y_{It}, respectively, which are well-known to follow a bivariate normal distribution (Henkelman,

[1] This is somewhat complicated by the work of Feng et al. (2009), who state that a non-zero (though small) phase change can be present in a region with randomly oriented vessels.

1985; Macovski, 1996; Wang and Lei, 1994). And, utilizing linear model structure, we define an $\boldsymbol{X}$ matrix (with tth row $\boldsymbol{x}_t'$) that models signal changes. In a simple setup with two columns, one column is an intercept modeling the baseline signal level and the other column models expected BOLD signal changes (Glover, 1999). Now, under a phase-coupled (PC) model, the real and imaginary means are connected by the phase location parameter θ_t; that is, $\mathbb{E}(y_{Rt}) = \boldsymbol{x}_t'\boldsymbol{\beta}\cos\theta_t$ and $\mathbb{E}(y_{It}) = \boldsymbol{x}_t'\boldsymbol{\beta}\sin\theta_t$. In contrast, the non-coupled (NPC) model does not connect these means, stating that $\mathbb{E}(y_{Rt}) = \boldsymbol{x}_t'\boldsymbol{\beta}_R$ and $\mathbb{E}(y_{It}) = \boldsymbol{x}_t'\boldsymbol{\beta}_I$. Non-phase-coupled approaches include complex-valued cross-correlation (Lai and Glover, 1997) and independent component analysis (Calhoun et al., 2002) and have been used in the steady-state free precession fMRI context (Lee et al., 2007). Phase-coupled approaches began with the assumption constant phase and magnitude-only activation (Nan and Nowak, 1999; Nencka and Rowe, 2007; Rowe and Logan, 2004) and were expanded to allow for task-related phase changes as well (Rowe, 2005a).

A distinct advantage of the PC approach is that it allows for separate tests of magnitude and phase task-related changes; the NPC approach only offers a test of combined magnitude/phase task-related changes in the complex plane. Given the previous discussion of the "brain or vein" problem, its implications in neurosurgical planning, and the use of phase task-related activation detection in discriminating between these two types of voxels, the separate magnitude and phase task-related tests offered by phase coupled models are valuable. Activation detection analysis based on the NPC model is somewhat easier to carry out, as parameter estimates follow from standard results. Early on, Rowe (2005a) utilized a Taylor approximation to simplify the PC model-based analysis, but the resulting parameter estimates may not fully maximize the likelihood function.

Later work in this area offers improvements to phase-coupled model implementation. First, a link function maps the angular range $-\pi$ to π to the unbounded linear predictor space (Fisher and Lee, 1992; Rowe et al., 2007). Additionally, the Adrian et al. (2018) model allows for temporal correlation within and cross correlation between the real and imaginary errors. In experimental data, these two types of correlation were shown to increase with the amount of spatial smoothing (see also Karaman et al., 2014; Nencka et al., 2009).

1.2 Contributions of this paper

In this paper, we improve on the phase-coupled complex-valued time series model for magnitude and phase task-related activation. Starting with the Rowe (2005a) model, we merge the Fisher and Lee (1992) link function and the Adrian et al. (2018) error structure to create a more general and reliable modeling framework. Further, we develop methodology for full ML estimation of the parameters and associated likelihood ratio tests for magnitude and phase activation. Section 2 provides methodological details regarding the statement of this model, estimation of its parameter, and implementation of hypothesis testing procedures. Section 3 presents the results of several simulation experiments showing the improved phase activation detection performance of this model performance over an uncoupled model and a phase-only data-based model. We close with a discussion in Section 4.

2. Methodology

Denote the real, imaginary, magnitude, and phase time series at a single voxel (suppressing subscripts for voxels) by $\boldsymbol{y}_R = (y_{R1}, \ldots, y_{Rn})'$, $\boldsymbol{y}_I = (y_{I1}, \ldots, y_{In})'$, $\boldsymbol{r} = (r_1, \ldots, r_n)'$, and $\boldsymbol{\phi} = (\phi_1, \ldots, \phi_n)'$, respectively, with n denoting the number of scans.

2.1 Models

The centerpiece of our methodological development is the following extension of the Rowe (2005a) model:

$$\begin{pmatrix} \boldsymbol{y}_R \\ \boldsymbol{y}_I \end{pmatrix} = \begin{pmatrix} \boldsymbol{C}\boldsymbol{X} & \boldsymbol{0} \\ \boldsymbol{0} & \boldsymbol{S}\boldsymbol{X} \end{pmatrix} \begin{pmatrix} \boldsymbol{\beta} \\ \boldsymbol{\beta} \end{pmatrix} + \begin{pmatrix} \boldsymbol{\eta}_R \\ \boldsymbol{\eta}_I \end{pmatrix}, \tag{1}$$

where $\boldsymbol{C}$ and $\boldsymbol{S}$ are $n \times n$ diagonal matrices with tth entries $\cos\theta_t$ and $\sin\theta_t$, respectively, $\boldsymbol{X}$ is an $n \times q_1$ matrix describing changes in the magnitude signal, and $\boldsymbol{\beta}$ is a q_1-vector. The errors $\boldsymbol{\eta} = (\boldsymbol{\eta}_R', \boldsymbol{\eta}_I')' \sim \mathcal{N}(\boldsymbol{0}, \boldsymbol{\Sigma} \otimes \boldsymbol{\Phi})$, where $\boldsymbol{\Sigma}$ and $\boldsymbol{\Phi}$ are matrices of order 2 and n, specifying the real/imaginary and temporal covariances, and the direct (Kronecker) product $\otimes$ implies separability of these covariances. For identifiability, we apply the constraint $\boldsymbol{X}\boldsymbol{\beta} \geq \boldsymbol{0}$. The phase parameters θ_t are modeled in terms of covariates $\boldsymbol{z}_t$ and corresponding parameters $\boldsymbol{\delta}$ (both q_2 vectors) as $\theta_t = \delta_0 + g(\boldsymbol{z}_t'\boldsymbol{\delta})$ with $g(\cdot) = 2\arctan(\cdot)$. As in Adrian et al. (2018), the matrix $\boldsymbol{\Sigma}$ is parameterized as $\boldsymbol{\Sigma}_{RR} = \sigma_R^2$, $\boldsymbol{\Sigma}_{II} = \sigma_I^2$, and $\boldsymbol{\Sigma}_{RI} = \rho\sigma_R\sigma_I$. Further, $\Phi = \boldsymbol{R}_n$ is specified by the AR(p) parameters $\boldsymbol{\alpha} = (\alpha_1, \ldots, \alpha_p)$. Denoting the model parameters by $\boldsymbol{\tau} = (\boldsymbol{\alpha}, \boldsymbol{\beta}, \delta_0, \boldsymbol{\delta}, \sigma_R^2, \sigma_I^2, \rho)$, model (1) has log-likelihood function given by

$$\log L(\boldsymbol{\tau}|\boldsymbol{y}_R, \boldsymbol{y}_I) = -n/2 \log[\sigma_R^2\sigma_I^2(1-\rho^2)] - \log|\boldsymbol{R}_n| - h/[2(1-\rho^2)], \tag{2}$$

where

$$h = \begin{pmatrix} \boldsymbol{\eta}_R \\ \boldsymbol{\eta}_I \end{pmatrix}' \begin{pmatrix} \frac{1}{\sigma_R^2}\boldsymbol{R}_n^{-1} & -\frac{\rho}{\sigma_R\sigma_I}\boldsymbol{R}_n^{-1} \\ -\frac{\rho}{\sigma_R\sigma_I}\boldsymbol{R}_n^{-1} & \frac{1}{\sigma_I^2}\boldsymbol{R}_n^{-1} \end{pmatrix} \begin{pmatrix} \boldsymbol{\eta}_R \\ \boldsymbol{\eta}_I \end{pmatrix}. \tag{3}$$

2.2 ML estimation

Maximum likelihood estimation of the model parameters consists of a mix of closed-form equations and Newton-Raphson steps. We present methods for obtaining starting values for the parameter estimates in Section 2.2.1 before presenting the ML equations in Section 2.2.2.

2.2.1 Starting values

Starting values $\delta_0^{(0)}$, $\boldsymbol{\beta}^{(0)}$, and $\boldsymbol{\delta}^{(0)}$ can be calculated as follows. First, $\delta_0^{(0)} = \arctan_4(s, c)$, where the $\arctan_4(y, x)$ is the 4-quadrant arctangent (see Glisson, 2011, Page 348) corresponding to $\arctan(y/x)$, $s = \sum_{t=1}^n r_t \sin\phi_t$ and $c = \sum_{t=1}^n r_t \cos\phi_t$. Second, $\boldsymbol{\beta}^{(0)} = (\boldsymbol{X}'\boldsymbol{X})^{-1}\boldsymbol{X}\boldsymbol{r}^*$, where $\boldsymbol{r}^*$ is an n-vector with tth entry $r_t^* = r_t\cos(\phi_t - \delta_0^{(0)})$. Last, $\boldsymbol{\delta}^{(0)}$ is calculated as $\boldsymbol{\delta}^{(0)} = \frac{1}{2}(\boldsymbol{Z}'\boldsymbol{W}\boldsymbol{Z})^{-1}\boldsymbol{Z}'\boldsymbol{v}$, where $\boldsymbol{W}$ is an n-diagonal matrix with tth entry $w_{tt} = \boldsymbol{x}_t'\boldsymbol{\beta}^{(0)} r_t\cos(\phi_t - \delta_0^{(0)})$ and $\boldsymbol{v}$ is an n-vector with tth entry $v_t = \boldsymbol{x}_t'\boldsymbol{\beta}^{(0)} r_t\sin(\phi_t - \delta_0^{(0)})$.

2.2.2 Estimation equations

Beginning with the starting values $\delta_0^{(0)}$, $\boldsymbol{\beta}^{(0)}$, and $\boldsymbol{\delta}^{(0)}$, MLEs for the parameters may be obtained by iteratively applying equations (4)-(10) until convergence of the log-likelihood function. The equations for σ_R^2, σ_I^2, and ρ are

$$\widehat{\sigma}_R^2 = (\boldsymbol{y}_R - \widehat{\boldsymbol{C}}\boldsymbol{X}\widehat{\boldsymbol{\beta}})'\widehat{\boldsymbol{R}}_n^{-1}(\boldsymbol{y}_R - \widehat{\boldsymbol{C}}\boldsymbol{X}\widehat{\boldsymbol{\beta}})/n \tag{4}$$

$$\widehat{\sigma}_I^2 = (\boldsymbol{y}_I - \widehat{\boldsymbol{S}}\boldsymbol{X}\widehat{\boldsymbol{\beta}})'\widehat{\boldsymbol{R}}_n^{-1}(\boldsymbol{y}_I - \widehat{\boldsymbol{S}}\boldsymbol{X}\widehat{\boldsymbol{\beta}})/n \tag{5}$$

$$\widehat{\rho} = (\boldsymbol{y}_R - \widehat{\boldsymbol{C}}\boldsymbol{X}\widehat{\boldsymbol{\beta}})'\widehat{\boldsymbol{R}}_n^{-1}(\boldsymbol{y}_I - \widehat{\boldsymbol{S}}\boldsymbol{X}\widehat{\boldsymbol{\beta}})/(n\widehat{\sigma}_R\widehat{\sigma}_I) \tag{6}$$

where $\widehat{\boldsymbol{C}}$ and $\widehat{\boldsymbol{S}}$ are n-diagonal matrices with tth elements $\cos\widehat{\theta}_t$ and $\sin\widehat{\theta}_t$, respectively, with $\widehat{\theta}_t = \widehat{\delta}_0 + g(\boldsymbol{z}_t'\widehat{\boldsymbol{\delta}})$. (In all cases, quantities with "hats" represent the most current estimates.) For the first iteration, $\boldsymbol{I}_n$ should be substituted for $\widehat{\boldsymbol{R}}_n^{-1}$; afterwards, $\widehat{\boldsymbol{R}}_n^{-1}$ is a $(2p+1)$-diagonal matrix that can be assembled from $\widehat{\boldsymbol{\alpha}}$ (see Pourahmadi, 2001, Section 4.4). Next, the equations for $\boldsymbol{\alpha}$ (Miller, 1995) are

$$\widehat{d}_{0i} = \sum_{j=1}^{p}[\widehat{d}_{ij} + (j/n)\widehat{d}_{0,|j-i|}]\widehat{\alpha}_j, \tag{7}$$

for $i = 1,\ldots,p$, where $\widehat{d}_{ij} = \widehat{d}_{ij}^{(RR)}/\widehat{\sigma}_R^2 + \widehat{d}_{ij}^{(II)}/\widehat{\sigma}_I^2 - \widehat{\rho}/(\widehat{\sigma}_R\widehat{\sigma}_I)[\widehat{d}_{ij}^{(RI)} + \widehat{d}_{ij}^{(IR)}]$, $0 \le i,j \le p$. In the previous, $\widehat{d}_{ij}^{(\iota\zeta)} = \sum_{t=1}^{n-i-j}\widehat{\eta}_{\iota,t+i}\widehat{\eta}_{\zeta,t+j}$ with $\iota,\zeta \in R,I$, with $\widehat{\eta}_{Rt} = y_{Rt} - \boldsymbol{x}_t'\widehat{\boldsymbol{\beta}}\cos\widehat{\theta}_t$ and $\widehat{\eta}_{It} = y_{It} - \boldsymbol{x}_t'\widehat{\boldsymbol{\beta}}\sin\widehat{\theta}_t$. Further, the equation for $\boldsymbol{\beta}$ is

$$\widehat{\boldsymbol{\beta}} = (\boldsymbol{X}'\widehat{\boldsymbol{A}}\boldsymbol{X})^{-1}\boldsymbol{X}'(\widehat{\boldsymbol{D}}\boldsymbol{y}_R + \widehat{\boldsymbol{E}}\boldsymbol{y}_I), \tag{8}$$

where the matrices $\widehat{\boldsymbol{A}}$, $\widehat{\boldsymbol{D}}$, and $\widehat{\boldsymbol{E}}$ are as follows: $\widehat{\boldsymbol{A}} = \widehat{\boldsymbol{C}}\widehat{\boldsymbol{R}}_n^{-1}\widehat{\boldsymbol{C}}/\widehat{\sigma}_R^2 + \widehat{\boldsymbol{S}}\widehat{\boldsymbol{R}}_n^{-1}\widehat{\boldsymbol{S}}/\widehat{\sigma}_I^2 - 2\widehat{\rho}\widehat{\boldsymbol{C}}\widehat{\boldsymbol{R}}_n^{-1}\widehat{\boldsymbol{S}}/(\widehat{\sigma}_R\widehat{\sigma}_I)$, $\widehat{\boldsymbol{D}} = [\widehat{\boldsymbol{C}}/\widehat{\sigma}_R^2 - \widehat{\rho}\widehat{\boldsymbol{S}}/(\widehat{\sigma}_R\widehat{\sigma}_I)]\widehat{\boldsymbol{R}}_n^{-1}$, and $\widehat{\boldsymbol{E}} = [\widehat{\boldsymbol{S}}/\widehat{\sigma}_I^2 - \widehat{\rho}\widehat{\boldsymbol{C}}/(\widehat{\sigma}_R\widehat{\sigma}_I)]\widehat{\boldsymbol{R}}_n^{-1}$. Note that it may be necessary to enforce the identifiability condition $\boldsymbol{X}\widehat{\boldsymbol{\beta}} \ge \boldsymbol{0}$, in which (8) will need to be modified as follows. The MLE of $\boldsymbol{\beta}$ subject to the constraint that $\boldsymbol{a}'\boldsymbol{\beta} = 0$ is $\tilde{\boldsymbol{\beta}} = \boldsymbol{\Psi}\widehat{\boldsymbol{\beta}}$, where $\boldsymbol{\Psi} = \boldsymbol{I}_{q_1} - (\boldsymbol{X}'\widehat{\boldsymbol{A}}\boldsymbol{X})^{-1}\boldsymbol{a}\boldsymbol{a}'/[\boldsymbol{a}'(\boldsymbol{X}'\widehat{\boldsymbol{A}}bX)^{-1}\boldsymbol{a}]$.

Newton-Raphson (NR) steps for δ_0 take the form

$$\delta_0^{(k+1)} = \delta_0^{(k)} - \left[\frac{\partial LL}{\partial\delta_0}(\delta_0^{(k)})\right] / \left[\frac{\partial^2 LL}{\partial\delta_0^2}(\delta_0^{(k)})\right], \tag{9}$$

where the first derivative and second partial derivatives are

$$\begin{aligned}
\frac{\partial LL}{\partial\delta_0} &= \boldsymbol{\beta}'\boldsymbol{X}(-\boldsymbol{M}_1\sin 2\delta_0 - \boldsymbol{M}_2\cos 2\delta_0)\boldsymbol{X}\boldsymbol{\beta} + 2\boldsymbol{\beta}'\boldsymbol{X}(\boldsymbol{m}_1\sin\delta_0 - \boldsymbol{m}_2\cos\delta_0) \\
\frac{\partial^2 LL}{\partial\delta_0^2} &= 2\boldsymbol{\beta}'\boldsymbol{X}(-\boldsymbol{M}_1\cos 2\delta_0 + \boldsymbol{M}_2\sin 2\delta_0)\boldsymbol{X}\boldsymbol{\beta} + 2\boldsymbol{\beta}'\boldsymbol{X}'(\boldsymbol{m}_1\cos 2\delta_0 + \boldsymbol{m}_2\sin 2\delta_0)
\end{aligned}$$

In the previous, $\boldsymbol{M}_1$ and $\boldsymbol{M}_2$ are $n\times n$ matrices given by $\boldsymbol{M}_1 = \left(\frac{1}{\sigma_R^2} - \frac{1}{\sigma_I^2}\right)(\tilde{\boldsymbol{C}}\boldsymbol{R}_n^{-1}\tilde{\boldsymbol{C}} - \tilde{\boldsymbol{S}}\boldsymbol{R}_n^{-1}\tilde{\boldsymbol{S}}) - \frac{2\rho}{\sigma_R\sigma_I}(\tilde{\boldsymbol{C}}\boldsymbol{R}_n^{-1}\tilde{\boldsymbol{S}} + \tilde{\boldsymbol{S}}\boldsymbol{R}_n^{-1}\tilde{\boldsymbol{C}})$ and $\boldsymbol{M}_2 = \left(\frac{1}{\sigma_R^2} - \frac{1}{\sigma_I^2}\right)(\tilde{\boldsymbol{C}}\boldsymbol{R}_n^{-1}\tilde{\boldsymbol{S}} - \tilde{\boldsymbol{S}}\boldsymbol{R}_n^{-1}\tilde{\boldsymbol{C}}) + \frac{2\rho}{\sigma_R\sigma_I}(\tilde{\boldsymbol{C}}\boldsymbol{R}_n^{-1}\tilde{\boldsymbol{C}} - \tilde{\boldsymbol{S}}\boldsymbol{R}_n^{-1}\tilde{\boldsymbol{S}})$. Further, $\boldsymbol{m}_1$ and $\boldsymbol{m}_2$ are vectors of length n given by $\boldsymbol{m}_1 = \boldsymbol{P}_{1R}\boldsymbol{R}_n^{-1}\boldsymbol{y}_R + \boldsymbol{P}_{1I}\boldsymbol{R}_n^{-1}\boldsymbol{y}_I$ and $\boldsymbol{m}_2 = \boldsymbol{P}_{2R}\boldsymbol{R}_n^{-1}\boldsymbol{y}_R + \boldsymbol{P}_{2I}\boldsymbol{R}_n^{-1}\boldsymbol{y}_I$, where $\boldsymbol{P}_{1R} = \frac{1}{\sigma_R^2}\tilde{\boldsymbol{C}} - \frac{\rho}{\sigma_R\sigma_I}\tilde{\boldsymbol{S}}$, $\boldsymbol{P}_{1I} = \frac{1}{\sigma_I^2}\tilde{\boldsymbol{S}} - \frac{\rho}{\sigma_R\sigma_I}\tilde{\boldsymbol{C}}$, $\boldsymbol{P}_{2R} - \frac{1}{\sigma_R^2}\tilde{\boldsymbol{S}} - \frac{\rho}{\sigma_R\sigma_I}\tilde{\boldsymbol{C}}$, and $\boldsymbol{P}_{2I} = \frac{1}{\sigma_I^2}\tilde{\boldsymbol{C}} + \frac{\rho}{\sigma_R\sigma_I}\tilde{\boldsymbol{S}}$. In the previous, $\tilde{\boldsymbol{C}}$ and $\tilde{\boldsymbol{S}}$ are n-diagonal matrices with tth entries $\cos g(\boldsymbol{z}_t'\boldsymbol{\delta})$ and $\sin g(\boldsymbol{z}_t'\boldsymbol{\delta})$, respectively.

Last, NR steps for $\boldsymbol{\delta}$ are

$$\boldsymbol{\delta}^{(k+1)} = \boldsymbol{\delta}^{(k)} - \left[\frac{\partial^2 LL}{\partial\boldsymbol{\delta}^2}(\boldsymbol{\delta}^{(k)})\right]^{-1}\left[\frac{\partial LL}{\partial\boldsymbol{\delta}}(\boldsymbol{\delta}^{(k)})\right] \tag{10}$$

Derivatives of the log-likelihood function w.r.t. $\boldsymbol{\delta}$ only concern the h function in (3), which can be written as $h = \sum_{t=1}^{n}\sum_{k=-p}^{p}\sum_{\iota,\zeta}c_{\iota\zeta}\boldsymbol{R}_n^{-1}(t,t+k)\eta_{\iota t}\eta_{\zeta,t+k}$. In the previous, ι and ζ are both summed over $\{R,I\}$, and $c_{\iota\zeta}$ is a constant not dependent of $\boldsymbol{\delta}$ (for instance, $c_{RR} = 1/\sigma_R^2$). Since the entries of $\boldsymbol{R}_n^{-1}$ also do not depend on $\boldsymbol{\delta}$, we need only concern ourselves with the derivatives of $\eta_{\iota t}\eta_{\zeta,t+k}$ w.r.t. $\boldsymbol{\delta}$ for $\iota,\zeta \in \{R,I\}$. The first derivative

$\partial/\partial\boldsymbol{\delta}(\eta_{\iota t}\eta_{\zeta,t+k}) = \eta_{\iota t}\eta'_{\zeta,t+k} + \eta'_{\iota t}\eta_{\zeta,t+k}$,[2] where $\eta'_{\iota t} = \rho_t \boldsymbol{z}_t g'(\boldsymbol{z}'_t\boldsymbol{\delta})(sc)_t$, with $(sc)_t = \mathbf{1}(\iota = R)\sin\theta_t - \mathbf{1}(\iota = I)\cos\theta_t$, where $\mathbf{1}(A)$ is the indicator function taking the value 1 of A is true and 0 otherwise. The second derivative $\partial^2/\partial\boldsymbol{\delta}^2(\eta_{\iota t}\eta_{\zeta,t+k}) = \eta_{\iota t}\eta''_{\zeta,t+k} + \eta''_{\iota t}\eta_{\zeta,t+k} + 2\eta'_{\iota t}\eta'_{\zeta,t+k}$, where $\eta''_{\iota t} = \rho_t \boldsymbol{z}_t \boldsymbol{z}'_t[g''(\boldsymbol{z}'_t\boldsymbol{\delta}) + g'(\boldsymbol{z}'_t\boldsymbol{\delta})(sc)'_t]$, with $(sc)'_t = \mathbf{1}(\iota = R)\cos\theta_t + \mathbf{1}(\iota = I)\sin\theta_t$.

2.3 Competing models

For simplicity, we do not distinguish notationally between corresponding terms in the different models in the following.

2.3.1 Uncoupled phase model

Lee et al. (2007) present the uncoupled phase model for complex-valued time series

$$[\boldsymbol{y}_R \vdots \boldsymbol{y}_I] = \boldsymbol{X}[\boldsymbol{\beta}_R \vdots \boldsymbol{\beta}_I] + [\boldsymbol{\eta}_R \vdots \boldsymbol{\eta}_I], \tag{11}$$

where $(\boldsymbol{\eta}'_R, \boldsymbol{\eta}'_I)' \sim \mathcal{N}(\mathbf{0}, \boldsymbol{\Sigma} \otimes \boldsymbol{I}_n)$. This is the multivariate multiple regression model $\boldsymbol{y} = \boldsymbol{X}\boldsymbol{\beta} + \boldsymbol{\eta}$ (see Johnson and Wichern, 2007, Section 7.7), where $\boldsymbol{y} = [\boldsymbol{y}_R \vdots \boldsymbol{y}_I]$ and $\boldsymbol{\eta} = [\boldsymbol{\eta}_R \vdots \boldsymbol{\eta}_I]$ are $n \times 2$ matrices and $\boldsymbol{\beta} = [\boldsymbol{\beta}_R \vdots \boldsymbol{\beta}_I]$ is a $q \times 2$ matrix. The MLEs are given by

$$\widehat{\boldsymbol{\beta}} = (\boldsymbol{X}'\boldsymbol{X})^{-1}\boldsymbol{X}'\boldsymbol{y} \tag{12}$$

$$\widehat{\boldsymbol{\Sigma}} = (\widehat{\boldsymbol{\eta}}'\widehat{\boldsymbol{\eta}})/n \tag{13}$$

Lee et al. (2007) present a Hotelling T^2 test statistic for the test of $H_0 : \boldsymbol{\beta}'\boldsymbol{a} = \mathbf{0}$ vs. $H_a : \boldsymbol{\beta}'\boldsymbol{a} \neq \mathbf{0}$, given by

$$T^2 = (\widehat{\boldsymbol{\beta}}'\boldsymbol{a})' \left[\frac{n}{n-q}\boldsymbol{a}'(\boldsymbol{X}'\boldsymbol{X})^{-1}\boldsymbol{a}\widehat{\boldsymbol{\Sigma}}\right]^{-1} (\widehat{\boldsymbol{\beta}}'\boldsymbol{a}), \tag{14}$$

which follows a $2(n-q)/(n-q-1)F_{2,n-q-1}$ null distribution. Rowe (2009) and Lee et al. (2009) discuss the similarities and differences between the coupled and uncoupled phase models.

2.3.2 Phase-only data-based regression model

The model assumes that each phase measurement ϕ_t is independent and follows the von-Mises distribution (Mardia and Jupp, 2000; von Mises, 1918) with location parameter $\theta_t = \delta_0 + g(\boldsymbol{z}'_t\boldsymbol{\delta})$ and concentration parameter κ, with $g(\cdot)$ and $\boldsymbol{z}'_t$ as before. Thus, the log-likelihood function is given by

$$\log L(\delta_0, \boldsymbol{\delta}, \kappa|\boldsymbol{\phi}) = -n\log(2\pi\mathbb{I}_0(\kappa)) + \kappa\sum_{t=1}^{n}\cos(\phi_t - \theta_t), \tag{15}$$

where $\mathbb{I}_0(\cdot)$ is defined as the modified Bessel function of the first kind and the zeroth order (Abramowitz and Stegun, 1965). An iterative algorithm for ML parameter estimation based on Fisher and Lee (1992); Rowe et al. (2007) is as follows: after calculating the starting

[2] denoting "prime" by partial derivative w.r.t. $\boldsymbol{\delta}$

value $\boldsymbol{\delta}^{(0)} = 0.5(\boldsymbol{W}'\boldsymbol{W})^{-1}\boldsymbol{W}'\boldsymbol{\phi}$, calculate the updated parameter estimates on iteration k as

$$\begin{aligned} \delta_0^{(k+1)} &= \arctan_4(S, C) && (16) \\ \kappa^{(k+1)} &= \mathbb{A}^{-1}(R) && (17) \\ \boldsymbol{\delta}^{(k+1)} &= \boldsymbol{\delta}^{(k)} + (\boldsymbol{Z}'\boldsymbol{G}^2\boldsymbol{Z})^{-1}\boldsymbol{Z}'\boldsymbol{G}^2\boldsymbol{w}. && (18) \end{aligned}$$

In (16), $S = (1/n)\sum_{t=1}^{n}\sin(\phi_t - g(\boldsymbol{z}_t'\boldsymbol{\delta}))$ and $C = (1/n)\sum_{t=1}^{n}\cos(\phi_t - g(\boldsymbol{z}_t'\boldsymbol{\delta}))$. In (17), $R = [S^2 + C^2]^{1/2}$ and $\mathbb{A}^{-1}(\cdot)$ is the inverse of the ratio of modified Bessel functions $\mathbb{A}(\cdot) = \mathbb{I}_1(\cdot)/\mathbb{I}_0(\cdot)$. The latter can be well approximated (Mardia and Jupp, 2000) as

$$\mathbb{A}^{-1}(R) \approx \begin{cases} 2R + R^3 + 5R^5/6 & R < 0.53 \\ -0.4 + 1.39R + 0.43/(1-R) & 0.53 \le R < 0.85 \\ \left[2(1-R) - (1-R)^2 - (1-R)^3\right]^{-1} & R \ge 0.85 \end{cases} \quad (19)$$

Last, in (18), $\boldsymbol{G}$ is a diagonal matrix with entries $g'(\boldsymbol{z}_t'\boldsymbol{\delta}) = 2/(1 + (\boldsymbol{z}_t'\boldsymbol{\delta})^2)$, $t = 1, \ldots, n$, and $\boldsymbol{w}$ is an n-vector with tth entry $w_t = \sin(\phi_t - \theta_t)/[\mathbb{A}(\kappa)g'(\boldsymbol{z}_t'\boldsymbol{\delta})]$. Iterations should proceed until convergence of (15).

A Wald test statistic for $H_0 : \boldsymbol{\delta} = \boldsymbol{0}$ vs. $H_a : \boldsymbol{\delta} \neq \boldsymbol{0}$ can be calculated from the MLE $\widehat{\boldsymbol{\delta}}$ and its asymptotic covariance matrix

$$\mathrm{Var}(\widehat{\boldsymbol{\delta}}) = \frac{1}{\widehat{\kappa}\mathbb{A}(\widehat{\kappa})}\left\{(\boldsymbol{Z}'\boldsymbol{G}^2\boldsymbol{Z})^{-1} + \frac{(\boldsymbol{Z}'\boldsymbol{G}^2\boldsymbol{Z})^{-1}\boldsymbol{Z}'\boldsymbol{g}\boldsymbol{g}'\boldsymbol{Z}(\boldsymbol{Z}'\boldsymbol{G}^2\boldsymbol{Z})^{-1}}{n - \boldsymbol{g}'\boldsymbol{Z}(\boldsymbol{Z}'\boldsymbol{G}^2\boldsymbol{Z})^{-1}\boldsymbol{Z}'\boldsymbol{g}}\right\}, \quad (20)$$

as given in Fisher and Lee (1992), where $\boldsymbol{g}$ is a vector whose elements are the diagonal entries of $\boldsymbol{G}$.

3. Simulation experiments

Section 2 introduced three methods for detecting task-related phase activation in fMRI time series, including two complex-valued (CV) data-based approaches that differ in whether the model couples the phase and the magnitude signals and an additional approach that utilizes the phase-only data (discarding the magnitude data). To compare these three methods in a setting of known ground truth, we performed simulation experiments. In all cases, we simulated CV time series according to model (1) where $\boldsymbol{X}$ and $\boldsymbol{Z}$ are specified according to a block design experiment with 16 time points of "off" followed by 19 epochs consisting 16 time points of "on" and 16 time points of "off". As a result, $\boldsymbol{X}$ has $n = 621$ rows (after discarding the first three time points to allow the scanner to come to equilibrium) and $q_1 = 2$ columns, the first of which is all ones and second models the expected BOLD response, calculated as the stimulus time course convolved with the Glover (1999) hemodynamic response function, which is then zero-centered and scaled to have maximum absolute value of one. The single column constituting $\boldsymbol{Z}$ is equal to the second column of $\boldsymbol{X}$, which follows the empirical observation of a linear relationship between magnitude and phase activation (Menon, 2002).

We simulated independent CV time series, that is, without AR temporal dependence and with real/imaginary error correlation $\rho = 0$; further, we assumed equality of real and imaginary error variances – *i.e.*, $\sigma_R^2 = \sigma_I^2 = 1$. Within this context, we performed two experiments. The first assumed no magnitude activation (*i.e.*, $\beta_1 = 0$ but varied the size of the phase activation parameter δ and compared the power of the three phase activation detection methods. Conversely, the second experiment assumed no phase activation but varied the size of the magnitude activation and compared the false positive rates of the

phase detection methods. In both experiments, we also varied the (magnitude) signal-to-noise ratio (SNR) β_0/σ from 0.5 to 10. In all cases, we generated 10,000 CV time series at each unique set of parameter values.

3.1 Phase activation power in the absence of magnitude activation

For the generated CV time series with no magnitude activation, we varied the size of the phase activation parameter δ from 0 to 0.04 radians. For each time series, we performed the phase activation test of under the three methods (CV coupled, CV uncoupled, and phase only) and calculated the proportion of time series detecting phase activation at the 0.001 significance level (the power). Figure 1(a) summarizes how the power of the phase activation test varies by δ, SNR, and method. Of course, the power increases with the phase

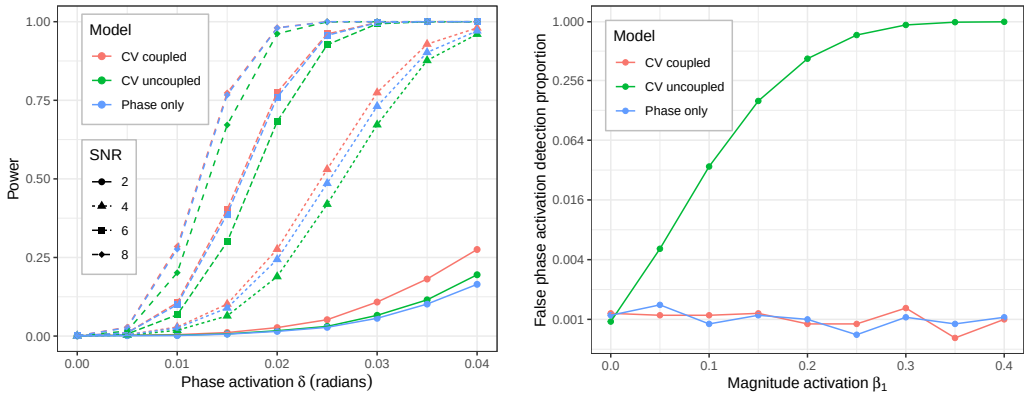

(a) Power

(b) False positive rate

Figure 1: (a) Phase activation detection power of simulated fMRI time series of varying phase activation parameters δ and (magnitude) SNRs. The proposed CV coupled model-based test is more powerful than existing CV uncoupled model-based and phase-only data-based tests. (b) The CV uncoupled model-based test fails to control the false phase activation detection rate at the significance level of 0.001 – it increases with the size of magnitude activation – unlike the CV coupled- and phase-only data-based tests.

activation size δ, but, for the same δ, it also increases with the SNR. The follows from the fact that the distribution of $\phi_t|r_t$ is von-Mises with location θ_t and concentration parameter $r_t\mu_t/\sigma = r_t\text{SNR}$. In other words, the (magnitude) SNR also affects the amount of "noise" in the phase distribution: the larger the SNR, the more concentrated the phase distribution (*i.e.*, less noise), leading to larger phase activation detection power. Comparing by method, the CV coupled model-based test has greater power in all cases. Its superiority over the phase-only data-based test can be attributed to its use of additional magnitude information; the size of this difference increases as the SNR decreases.[3] Further, the superior power of the CV coupled- vis-a-vis the uncoupled model-based test can be attributed to "specificity". The coupled model-based phase activation test $H_0 : \delta = 0$ vs. $H_a : \delta \neq 0$ focuses only on the phase activation parameter, while the uncoupled model-based test $H_0 : (\beta_{R1}, \beta_{I1})' = \mathbf{0}$ vs. $H_a : (\beta_{R1}, \beta_{I1})' \neq \mathbf{0}$ tries to detect the same phase activation with two parameters, and therefore is less powerful.

[3] We can connect this result to previous results for magnitude activation detection: increased power for CV coupled model-based tests over magnitude-only data-based tests in the absence of phase activation (Adrian et al., 2018; Rowe and Logan, 2004).

3.2 False phase activation detection in the presence of magnitude activation

For the generated CV times with no phase activation, we varied the size of the magnitude activation parameter β_1 from 0 to 0.4. Figure 1(b) displays the proportion of time series detecting phase activation at the 0.001 significance level (the false positive rate) at SNR = 6.While the methods which test the phase activation parameter δ – the CV coupled model-based and phase-only data-based tests – have false positive rates adhering with the significance level (after accounting for simulation variability), the false positive rate of the CV uncoupled model-based test grows with the size of the magnitude activation. This is because the CV uncoupled model-based test detects any change in the CV signal, whether it arises in the magnitude or phase direction, or both.

4. Discussion

In this article, we have presented a novel model for magnitude and phase activation in fMRI time series and illustrated estimation of its parameters. The phase-coupled structure of this model provides separate tests of activation for the magnitude and the phase data, which show promise in the "brain or vein" problem", distinguishing voxels that show neuronal activation from neighboring voxels containing draining veins. Such distinguishing ability could prove essential for fMRI applications in neurosurgical planning. Simulation experiments indicate that, in comparison to complex-valued phase-uncoupled and phase-only data-based models, our phase-coupled model shows increased power of detecting phase activation in the absence of magnitude activation and is not prone to false positives in phase activation detection in the presence of magnitude activation.

References

Abramowitz, M. and I. Stegun (1965). *Handbook of Mathematical Functions*. Dover Publications.

Adrian, D. W., R. Maitra, and D. B. Rowe (2018). Complex-valued time series modeling for improved activation detection in fMRI studies. *Annals of Applied Statistics 12*(3), 1451–1478.

Bandettini, P. A., A. Jesmanowicz, E. C. Wong, and J. S. Hyde (1993). Processing strategies for time-course data sets in functional MRI of the human brain. *Magnetic Resonance in Medicine 30*, 161–173.

Belliveau, J. W., D. N. Kennedy, R. C. McKinstry, B. R. Buchbinder, R. M. Weisskoff, M. S. Cohen, J. M. Vevea, T. J. Brady, and B. R. Rosen (1991). Functional mapping of the human visual cortex by magnetic resonance imaging. *Science 254*, 716–719.

Brown, T. R., B. M. Kincaid, and K. Ugurbil (1982). NMR chemical shift imaging in three dimensions. In *Proceedings of the National Academy of Sciences, USA*, Volume 79, pp. 3523–3526.

Calhoun, V. D., T. Adali, G. D. Pearlson, P. van Zijl, and J. J. Pekar (2002). Independent component analysis of fMRI data in the complex domain. *Magnetic Resonace in Medicine 48*, 180–192.

Duvernoy, H. M. (1999). *The human brain: surface, blood supply, and three-dimensional sectional anatomy* (Second edition ed.). Springer-Verlag.

Feng, Z., A. Caprihan, K. B. Blagoev, and V. D. Calhoun (2009). Biophysical modeling of phase changes in bold fMRI. *NeuroImage 47*, 540–548.

Fisher, N. I. and A. J. Lee (1992). Regression models for an angular response. *Biometrics 48*, 665–677.

Frahm, J., K. D. Merboldt, W. Hanicke, A. Kleinschmidt, and H. Boecker (1994). Brain or vein-oxygenation or flow? on signal physiology in functional MRI of human brain activation. *NMR in Biomedicine 7*(3), 45–53.

Glisson, T. H. (2011). *Introduction to Circuit Analysis and Design*. The Netherlands: Springer.

Glover, G. H. (1999). Deconvolution of impulse response in event-related BOLD fMRI. *NeuroImage 9*, 416–429.

Haacke, E. M., Y. Xu, Y. C. Cheng, and J. R. Reichenbach (2004). Susceptibility weighted imaging (SWI). *Magnetic Resonance in Medicine 52*(3), 612–618.

Henkelman, R. M. (1985). Measurement of signal intensities in the presence of noise in MR images. *Medical Physics 12*, 232–233.

Hoogenrad, F. G., J. R. Reichenbach, E. M. Haacke, S. Lai, K. Kuppusamy, and M. Sprenger (1998). In vivo measurement of changes in venous blood-oxygenation with high resolution functional MRI at .95 Tesla by measuring changes in susceptibilty and velocity. *Magnetic Resonace in Medicine 39*, 97–107.

Jain, A. K. (1989). *Fundaments of Digital Image Processing*. Prentice Hall.

Jezzard, P. and S. Clare (2001). Principles of nuclear magnetic resonance and MRI. In P. Jezzard, P. M. Matthews, and S. M. Smith (Eds.), *Functional MRI: An Introduction to Methods*, Chapter 3, pp. 67–92. Oxford University Press.

Johnson, R. A. and D. W. Wichern (2007). *Applied Multivariate Statistical Analysis* (Sixth edition ed.). Pearson.

Karaman, M., A. S. Nencka, I. P. Bruce, and D. B. Rowe (2014). Quantification of the statistical effect of spatiatemporal processing of nontask fMRI data. *Brain Connectivity 4*(9), 649–661.

Kwong, K. K., J. W. Belliveau, D. A. Chesler, I. E. Goldberg, R. M. Weisskoff, B. P. Poncelet, D. N. Kennedy, B. E. Hoppel, M. S. Cohen, R. Turner, H.-M. Cheng, T. J. Brady, and B. R. Rosen (1992). Dynamic magnetic resonance imaging of human brain activity during primary sensory stimulation. *Proceedings of the National Academy of Sciences of the United States of America 89*, 5675–5679.

Lai, S. and G. H. Glover (1997). Detection of BOLD fMRI signals using complex data. In *ISMRM*, pp. 1671.

Lazar, N. A. (2008). *The Statistical Analysis of Functional MRI Data*. Springer.

Lee, C. C., C. R. Jack, and S. J. Riederer (1998). Mapping of the central sulcus with functional MR: Active versus passive activation tasks. *American Journal of Neuroradiology 19*, 847–852.

Lee, C. C., H. A. Ward, F. W. Sharbrough, F. B. Meyer, W. R. Marsh, C. Raffel, E. L. So, G. D. Cascino, C. Shin, Y. Xu, S. J. Riederer, and C. R. Jack (1999). Assessment of functional MR imaging in neurosurgical planning. *American Journal of Neuroradiology 20*, 1511–1519.

Lee, J., M. Shahram, and J. M. Pauly (2009). Combining complex signal change in functional MRI. *Magnetic Resonance in Medicine 62*(5), 1358–1360.

Lee, J., M. Shahram, A. Schwartzman, and J. M. Pauly (2007). Complex data analysis in high-resolution SSFP fMRI. *Magnetic Resonance in Medicine 57*, 905–917.

Ljunggren, S. (1983). A simple graphical representation of Fourier-based imaging methods. *Journal of Magnetic Resonance 54*, 338–343.

Macovski, A. (1996). Noise in MRI. *Magnetic Resonance in Medicine 36*(3), 494–497.

Mardia, K. V. and P. E. Jupp (2000). *Directional Statistics*. Wiley.

Menon, R. S. (2002). Postacquisition suppression of large-vessel BOLD signals in high-resolution fMRI. *Magnetic Resonace in Medicine 47*, 1–9.

Miller, J. W. (1995). Exact maximum likelihood estimation in autoregressive processes. *Journal of Time Series Analysis 16*, 607–615.

Nan, F. Y. and R. D. Nowak (1999). Generalized likelihood ratio detection for fMRI using complex data. *IEEE Transactions on Medical Imaging 18*, 320–329.

Nencka, A. S., A. D. Hahn, and D. B. Rowe (2009). A Mathematical Model for Understanding the STatistical effects of k-space (AMMUST-k) preprocessing on observed voxel measurements in fcMRI and fMRI. *Journal of Neuroscience Methods 181*, 268–282.

Nencka, A. S., E. S. Paulson, and D. B. Rowe (2008). Complex constant phase statistical model reduces venous contributions to BOLD cortical activations in the visual cortex. In *Proceedings of ISMRM*, pp. 2338.

Nencka, A. S. and D. B. Rowe (2007). Reducing the unwanted draining vein BOLD contribution in fMRI with statistical post-processing methods. *NeuroImage 37*, 177–188.

Ogawa, S., T. M. Lee, A. S. Nayak, and P. Glynn (1990). Oxygenation-sensitive contrast in magnetic resonance image of rodent brain at high magnetic fields. *Magnetic Resonance in Medicine 14*, 68–78.

Pillai, J. J. (2010). The evolution of clinical functional imaging during the past 2 decades and its current impact on neurosurgical planning. *American Journal of Neuroradiology 31*, 219–225.

Pourahmadi, M. (2001). *Foundations of Time Series Analysis and Prediction Theory*. Wiley.

Reichenbach, J. R. (2012). The future of susceptibility contrast for assessment of anatomy and function. *NeuroImage 62*, 1311–1315.

Reichenbach, J. R., R. Venkatesan, D. J. Schillinger, D. K. Kido, and E. M. Haacke (1997). Small vessels in the human brain: MR venography with deoxyhemoglobin as an intrinsic contrast agent. *Radiology 204*(1), 272–277. PMID: 9205259.

Rowe, D. B. (2005a). Modeling both the magnitude and phase of complex-valued fMRI data. *NeuroImage 25*, 1310–1324.

Rowe, D. B. (2005b). Parameter estimation in the magnitude-only and complex-valued fMRI data models. *NeuroImage 25*, 1124–1132.

Rowe, D. B. (2009). Magnitude and phase signal detection in complex-valued fMRI data. *Magnetic Resonance in Medicine 62*(5), 1356–1357.

Rowe, D. B. and E. M. Haacke (2009). MAgnitude and PHase Thresholding (MAPHT) of noisy complex-valued magnitude resonance images. *Magnetic Resonance Imaging 27*(9), 1271–1280.

Rowe, D. B. and B. R. Logan (2004). A complex way to compute fMRI activation. *NeuroImage 23*, 1078–1092.

Rowe, D. B. and B. R. Logan (2005). Complex fMRI analysis with unrestricted phase is equivalent to a magnitude-only model. *NeuroImage 24*, 603–606.

Rowe, D. B., C. P. Meller, and R. G. Hoffman (2007). Characterizing phase-only fMRI data with an angular regression model. *Journal of Neuroscience Methods 161*, 331–341.

Tweig, D. B. (1983). The k-trajectory formulation of the NMR imaging process with applications in analysis and synthesis of imaging methods. *Medical Physics 10*(5), 610–21.

von Mises, R. (1918). Uber die 'ganzzahligkeit' der atomgewichte und verwandte fragen. *Physaikalische Zeitschrift 19*, 490–500.

Wang, T. and T. Lei (1994, April). Statistical analysis of MR imaging and its applications in image modeling. *Proceedings of the IEEE International Conference on Image Processing and Neural Networks 1*, 866–870.